



REVIEW ARTICLE

Fabrication of Metal and Alloy Components by Additive Manufacturing: Examples of 3D Materials Science

Lawrence E. Murr^{1,2,*}, Edwin Martinez^{1,2}, Krista N. Amato^{1,2}, Sara M. Gaytan^{1,2}, Jennifer Hernandez^{1,2}, Diana A. Ramirez^{1,2}, Patrick W. Shindo^{1,2}, Frank Medina², Ryan B. Wicker²

¹Department of Metallurgical and Materials Engineering, The University of Texas at El Paso, El Paso, TX 79968 USA.

²W. M. Keck Center for 3D Innovation, The University of Texas at El Paso, El Paso, TX 79968 USA.

Manuscript received April 3rd, 2012; in revised form April 18, 2012



Lawrence E. Murr is Mr. & Mrs. MacIntosh Murchison Professor and Chairman of the Department of Metallurgical and Materials Engineering and Ph.D. Program Director in the Materials Research & Technology Institute at The University of Texas at El Paso. Dr. Murr received his B.Sc. in physical science from Albright College, and his B.S.E.E. in electronics, his M.S. in engineering mechanics, and his Ph.D. in solid-state science, all from the Pennsylvania State University. Dr. Murr has published 20 books, over 775 scientific and technical articles in a wide range of research areas in materials science and engineering, environmental science and engineering, manufacturing science and engineering, and biological sciences and engineering; roughly half with undergraduate and graduate student researchers. During nearly a half-century of university teaching, Professor Murr has also directed 65 M.S. theses and 35 Ph.D. dissertations. Recent honors include the 2001 Buehler Technical Paper Merit Award for Excellence (IMS), the TMS 2007 Educator Award, the 2007 John S. Rinehart Award (a TMS Symposium Award for global leadership in shock and high-strain-rate phenomena), and the 2008 Henry

Clifton Sorby Award presented by the International Metallographic Society (IMS) for recognition of lifetime achievement in the field of metallurgy. In 2009, Professor Murr received the Albert Easton White Distinguished Teacher Award from ASM International. Dr. Murr was also awarded a Lee Hsun Research Award by the Shenyang National Laboratory for Materials Science, Institute of Metal Research, Chinese Academy of Sciences (IMR-CAS) "in recognition of past accomplishments in materials science and technology" (2009-2010). In 2010, Professor Murr was honored as a Visiting Professor for Senior International Scientists by the Chinese Academy of Sciences (CAS) for the Institute of Metal Research (IMR) of the Shenyang National Laboratory (SYNL) for Materials Science. Professor Murr was chosen for a Piper Professor of 2010 Award for "Outstanding scholarly achievements and superior teaching at the college level", a Texas higher education program of the Minnie Stevens Piper Foundation. Professor Murr is also a Fellow of ASM International and a licensed professional engineer.

Objective: This paper provides a brief review of relatively new additive manufacturing technologies for the fabrication of unusual and complex metal and alloy products by laser and electron beam melting. A number of process features and product microstructures are illustrated utilizing 3D optical and transmission electron microscope image compositions representing examples of 3D materials science. **Methods:** Processing methods involving electron beam melting (EBM) and a process referred to as direct metal laser sintering

*Corresponding author.

E-mail address: lemurr@utep.edu (L. E. Murr)

(DMLS), often called selective laser melting (SLM) are described along with the use of light (optical) microscopy (OM), transmission electron microscopy (TEM), and X-ray diffraction (XRD) to elucidate microstructural phenomena. Results: Examples of EBM and SLM studies are presented in 3D image compositions. These include EBM of Ti-6Al-4V, Cu, Co-base superalloy and Inconel 625; and SLM of 17-4 PH stainless steel, Inconel 718 and Inconel 625. Conclusions: 3D image compositions constituting 3D materials science provide effective visualization for directional solidification-related phenomena associated with the EBM and SLM fabrication of a range of metals and alloys, especially microstructures and microstructural architectures.

KEY WORDS: Laser and electron beam melting; 3D image compositions; Optical and electron microscopy; Metal and alloy fabrication; Microstructures

© 2012 Brazilian Metallurgical, Materials and Mining Association. Published by Elsevier Editora Ltda.

Este é um artigo Open Access sob a licença de [CC BY-NC-ND](https://creativecommons.org/licenses/by-nc-nd/4.0/)

1. Introduction

The concept of advanced manufacturing technology (AMT) has been viewed as encompassing or utilizing computer and numerical-based processing or fabrication of materials^[1]. These have included CNC, CAD and more recently three-dimensional (3D) printing and related layer-by-layer fabrication or additive manufacturing (AM)^[2-4]. Particularly promising AM technologies involve CAD-driven laser or electron beam melting where complex 3D CAD models direct selective melting of metal or pre-alloyed powder layers forming near-net-shaped components requiring little final machining or finishing; with correspondingly little waste since unmelted powder within and around the AM product is recovered and recycled^[3].

AM, often referred to as 3D printing, builds a solid, often geometrically complex object from a series of layers each one “printed” on top of the previous one. In contrast to more conventional, “subtractive” processes such as CNC milling or machining to remove up to 95% of material from billets, forgings, or castings to create the product, AM systems capable of printing functional components require no tooling and, as noted above, produce minimal waste. While additive fabrication implies the process itself, AM refers to additive fabrication technologies utilized to manufacture prototypes and finished parts used in the final product. These technologies range from aerosol jetting of molecular precursors or nanoparticulate’s suspensions to print layers which are post treated with focused laser beams to remove the binder and sinter the nanomaterials, to the raking or rolling of micron-size powders into layers which are selectively preheated and melted one layer over the other to build 3D products.

In this paper we review recent progress in the characterization and analysis of AM prototypes fabricated by laser and electron beam melting technologies, referred to as direct metal laser sintering (DMLS) or selective laser melting (SLM) and electron beam melting (EBM), respectively^[5-13]. In reviewing these technology prototypes, a variety of metal and alloy components are illustrated utilizing 3D materials science examples^[14] to characterize and visualize the development of novel and unusual microstructures and microstructural architectures resulting from successive layer melt-solidification phenomena. Particularly visual image compositions include 3D light optical metallographic (LOM) and electron microscopy observations for SLM and EBM fabricated metal or alloy components.

2. Laser and Electron Beam Melting Technologies

Fig. 1 illustrates the physical features of the Arcam A2 EBM system. The computer control and recording section is located on the left while the right portion (indicated by EBM at the arrow) houses the electron beam forming and processing system. This system, shown schematically in Fig. 2a, resembles a typical electron optical column similar to an electron beam welder or a scanning electron microscope where an electron gun at (1) generates the initial electron beam accelerated at 60 kV potential through a focusing lens system (2) and a magnetic scanning coil system at (3). The focused electron beam is selectively scanned over the powder layer directed by an embedded CAD model. The powder layer is formed by raking gravity fed powder at (5) which flows from cassettes at (4). The component (6) is built by preheating and selectively melting each successive layer in the build direction shown by the arrow at B. The build table (7) is correspondingly lowered as shown by the large arrow opposite to the build direction. Processing in the EBM



Fig. 1 Arcam A2 EBM System. Arrow at top right indicates the electron beam melting/processing system. Control unit is at left

system is done in a background vacuum of 10^{-4} to 10^{-5} Torr. A helium bleed near the build area reduces the vacuum to $\sim 10^{-2}$ Torr and provides specimen cooling and beam scan stability.

In the EBM system, the preheating of the powder is achieved by successive, rapid scanning of the beam at high beam current. This achieves preheat, raked-layer temperatures of ~ 0.4 to $0.6 T_M$ (where T_M is the melting temperature). Following the preheat scanning, the melt scan rate is reduced by $\sim 10^2$ mm/s and the corresponding beam current reduced by roughly a factor of 5.

Since there is no changing of the powder bed by the laser beam there is no pre-heat or pre-melt scan in SLM. In addition, the coupling of the beam energy with the powder bed also differs for the electron beam in contrast to the laser beam.

As illustrated schematically in Fig. 2, the DMLS or SLM system is conceptually similar to the EBM system except that a laser beam (1) is scanned using a CAD-driven mirror system (2) and focused with conventional glass lenses (3). The powder is rolled (4) from a supply container (6) into a single layer similar to the raking in the EBM system in Fig. 1. Excess powder is collected at (7). As each layer is selectively melted, the build table drops down a corresponding layer as shown at (5) in Fig. 2b. In contrast to the EBM system in Fig. 1, the SLM system shown in Fig. 2b (corresponding to an EOS M270 machine) employs either a purified nitrogen or argon gas environment. Nitrogen poses an advantage in that its thermal conductivity is roughly 40% greater than that of the argon even at very high temperatures^[15]. This affords more rapid component cooling and solidification.

In the SLM (melt) processing of rolled, recoated powder layers the melt scan rate is usually two orders of magnitude greater than the EBM melt scan rate. This induces more rapid layer and component cooling and solidification. Consequently alloy systems whose microstructures are sensitive to solidification rates will respond differently to EBM processing in contrast to SLM processing.

Figs. 2c and 2d show two different schematic views for the formation of a melt surface composed of discrete melt pools created in the x-y beam scanning for both EBM (electron beam) and SLM (laser beam). The dimensions of these melt pools will depend upon the beam focus and scan rate as well as the coupling of the beam with the raked or rolled powder layer. Coupling differs for 60 kV electrons in contrast to energetic (laser) photons in a complex way, but the slowest scanned electron beam usually produces a larger melt pool dimension than the more rapidly scanned laser beam. Figs. 2c and 2d show columnar growth features near the center of the melt pools and cylindrical-like microstructural features at the melt pool edges, respectively; corresponding to temperature variances or gradients. The liquid/solid interface becomes a connected 2-dimensional array of distinct thermal gradients which produce directional microstructures: columnar or oriented (textured) grains and other directional microstructures simultaneously. Depending upon the specific thermo-kinetic variables, precipitation and related transformation phenomena may occur preferentially in the melt pool center or in the transition regions between melt pools as shown schematically in Figs. 2c and 2d, respectively. Thijs *et al.*^[16] have recently demonstrated that the development of microstructure of

Ti-6Al-4V alloy processed by SLM was influenced by scanning parameters and scanning strategy as well as the occurrence of epitaxial growth in the melt pools. The direction of elongated grains was shown to be directly related to the process parameters.

Table 1 compares build parameters and process conditions for EBM and SLM fabrication.

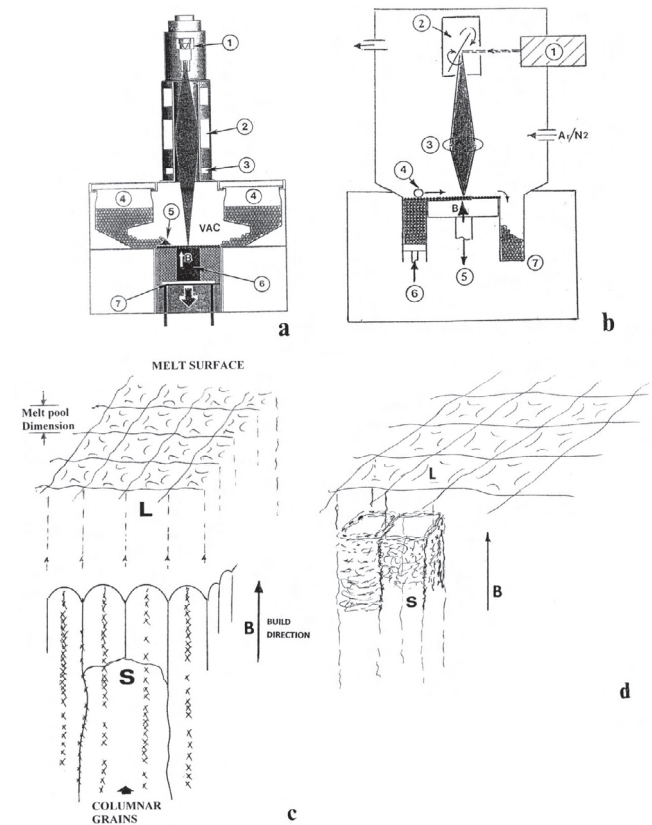


Fig. 2 (a) EBM and (b) SLM process schematic views. The EBM system shown at the arrow in Fig. 1 is represented schematically in (a). (c) and (d) show schematic representations of both EBM and SLM process features: the formation of the melt layer composed of discrete melt pools. In (c) columnar grains and melt pool center-oriented microstructures are shown. In (d) the columnar microstructures are associated with the melt pool edges. (a)–(c) adapted from Martinez *et al.*^[14]

Table 1 Build Parameters and Process Conditions for EBM and SLM Systems

Process/Parameters	EBM	SLM
Environment	Vacuum/He bleed	Ar or N ₂
Preheat Beam Passes	10–12	None
Preheat Scan Speed (beam)	10 ⁴ mm/s	—
Melt Scan Speed (beam)	10 ² mm/s	10 ⁴ mm/s
Preheat Beam Current	25–30 mA	—
Melt Scan Beam Current	4–8 mA	—
Beam/Melt Pool Dimension	2–3 μm	0.5–1.5 μm
Build speed	6–7 mm/h	7–8 mm/h

3. Powder Properties and Build Strategies

In both the EBM raking and SLM (or DMLS) rolling/recoating of successive powder layers (Figs. 2a and 2b), the properties of the powders are important. As in many powder-based production processes, the flow and corresponding layer packing of the powder dictates the efficiency in selective melting and the quality of the product. Powder flowability is a complex issue, and flow behavior is multidimensional and multivariable. Flow properties include density (or compressibility) cohesive strength and wall friction as well as van der Waals and electrostatic forces acting on the powder particles, surface tension and space filling or interlocking characteristics determined by the particle sizes or size distribution^[17-19]. Flowability improves significantly with sphericity, and irregular, crushed powders have poor flowability. However, Boulos^[20-22] has described the ability of induction plasma melting to create spherical powder particles from irregular, crushed precursor powders. This process can produce much cheaper powders than the more traditional atomization or rapid solidification processing (RSP) of metal or pre-alloyed powders. Powders for SLM usually work better for smaller sizes and distributions while bimodal distributions especially in EBM processing can promote layer filling and densification which improves beam energy coupling in both EBM and SLM processing.

As illustrated in Fig. 3, large, monosized particles contain larger interstitial voids which can be filled by smaller particle sizes while very small monosized particles can pack more efficiently, with less interstitial volume to fill. Considering that an average of three particle diameters (large unisized particle diameters) can create a contiguous, packed layer (Fig. 3c) the smaller particle size shown in Fig. 3b can form a layer half or correspondingly less in thickness. In the absence of smaller size or distributed particle sizes, sinterability and melting are more readily achieved for the smaller particles in Fig. 3b than the larger ones in Fig. 3c, although smaller, distributed sizes which fill the interstitial

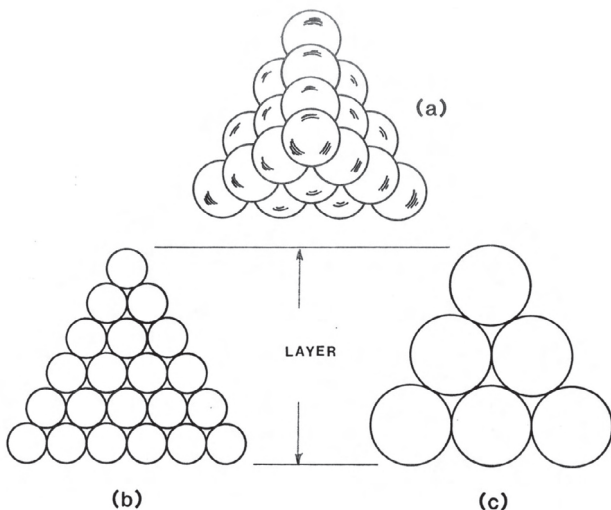


Fig. 3 Idealized powder packing: unisized particles. (a) Top view; (b) side view of layer packing with small particles; and (c) side view of layer packing with large particles

volumes will enhance sintering and melting. This is shown ideally for atomized Cu powder in Fig. 4b.

Fig. 4a illustrates the build process schematically where each successive powder layer is selectively melted to form a complex, 3D component. Fig. 4b illustrates, as noted above, an ideal EBM powder with a relatively bimodal size distribution of nearly perfect RSP spheres of copper, having an average particle size of $\sim 11 \mu\text{m}$. This size regime is also ideal for SLM processing as well. It can be noted in the build schematic of Fig. 4a that the unmelted powder in each layer can be recovered and recycled. However, complex, internal structures must have a powder outlet, and as a consequence closed-cellular products, even closed-cell foams, cannot be fabricated. Powder removal from complex components is usually affected by high-pressure air blasting, vibratory processing, or some combination of these. It may also be apparent from Fig. 4a that because of the layer melting and heat retention of built products, there are limitations in feature size: usually $\sim 100 \mu\text{m}$; roughly the layer thickness for routine EBM processing. Smaller feature sizes produce particle sintering in unmelted areas which prevents powder removal even for appropriately built components.

Since it is difficult to specifically measure beam size in either the EBM or SLM process, the strategy to optimize the beam size or the beam focal conditions employs a focus offset

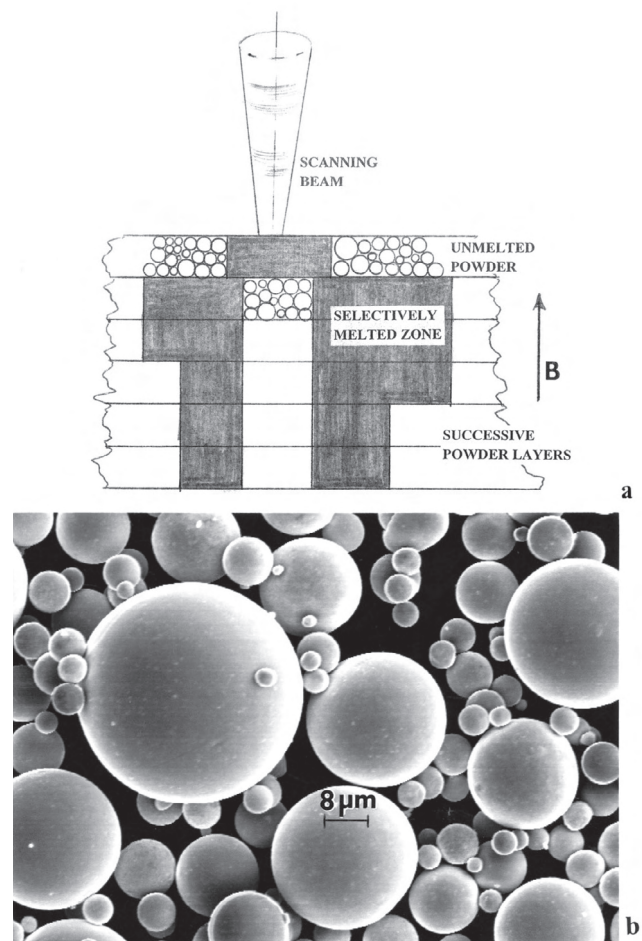


Fig. 4 Melt scan and selective powder layer melting to form complex part geometries (a) B shows the build direction; (b) shows essentially ideal, bimodal, copper atomized powder

where test blocks are systematically fabricated at different focus offset conditions, and the microstructures examined at some appropriate level of resolution. Fig. 5 illustrates this concept for EBM fabrication of Ti-6Al-4V test blocks. While the interior microstructures are examined for residual porosity (and unmelted powder zones) the grain or phase structures and structure sizes are also examined. In addition, the final melt surface roughness as shown in Fig. 5 is also an indicator of process optimization relative to focus offset.

Figs. 6 and 7 illustrate representative 3D microstructure compositions for the corresponding focus offset numbers shown in Fig. 5. The numbers noted in the horizontal and vertical plane sections to the left in each image composition represent the Vickers microindentation hardness (in GPa) average. The horizontal plane hardness is consistently higher than the vertical plane hardness and there are variations in the α -phase grain structure and size. In this analysis, focus offset 6 was considered the best build condition (Figs. 5 and 7).

Fig. 8 shows for comparison an optimized Ti-6Al-4V component fabricated by EBM and SLM. While the EBM microstructure in Fig. 8a shows the α -phase grain structure and β -boundary areas, the SLM microstructure in Fig. 8b is dominated by α' -martensite platelets. The arrows in Figs. 8a and 8b show columnar grain boundaries generally parallel to the build direction (B in Fig. 8b). The α' -martensite in Fig. 8b forms in preference to the acicular α -phase because of the more rapid solidification in SLM processing in contrast to EBM processing. It should be noted that the Vickers microindentation hardness (HV) for both Figs. 8a and 8b was 4.5 GPa in contrast to that for Figs. 6 and 7. This is due primarily to the α and β phase widths which are similar ($\sim 2 \mu\text{m}$) in Figs. 8a and 8b, but larger ($\sim 6 \mu\text{m}$) in Figs. 6 and 7; particularly in the vertical reference plane.

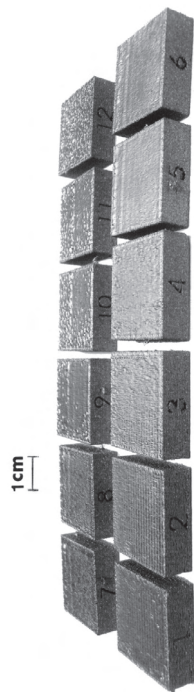


Fig. 5 Ti-6Al-4V optimization test block sequence for electron beam focus offset in EBM processing

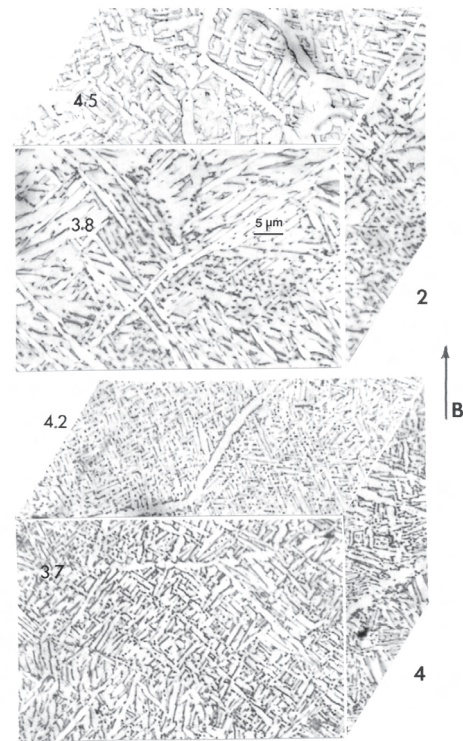


Fig. 6 Ti-6Al-4V 3D LOM image compositions corresponding to test block sections in Fig. 5. Numbers in horizontal and vertical reference planes at left are Vickers microindentation hardness in GPa. Numbers 2 and 4 at right refer to test block (focus offset) numbers in Fig. 5. B indicates the build direction

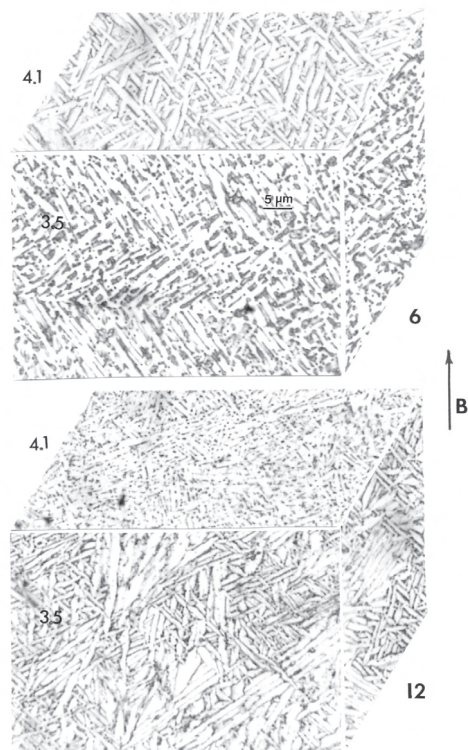


Fig. 7 Continuation of 3D LOM image compositions in Fig. 6, corresponding to test block sections in Fig. 5. Numbers in horizontal and vertical reference planes at left are Vickers microindentation hardness in GPa. Numbers 6 and 12 at right refer to test block (focus offset) numbers in Fig. 5. B indicates the build direction

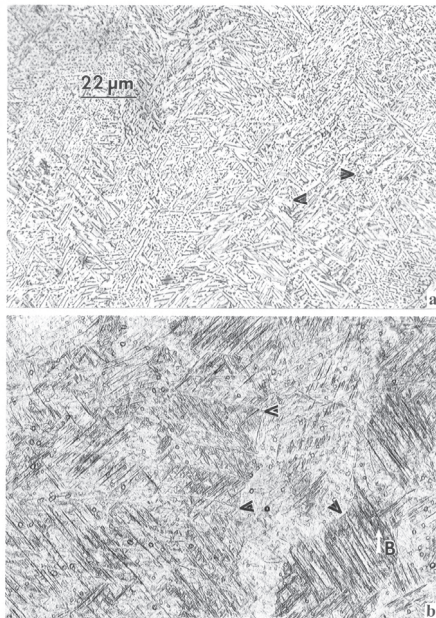


Fig. 8 Comparison of (a) EBM and (b) SLM microstructures for Ti-6Al-4V by LOM. (a) and (b) represent vertical reference sections, parallel to the build direction (shown at B in (b)). Arrow tips indicate columnar grain boundaries

4. EBM and SLM Fabricated Component Microstructures

4.1 EBM Fabricated Copper

Fig. 9 shows a 3D (isometric) LOM image composition of a section of an EBM-fabricated cylindrical copper component utilizing the precursor powder illustrated in Fig. 4b. The horizontal surface reference plane shows a regular, cell-like array having a diameter of 2–3 μm diameter corresponding to the typical melt-pool dimension (Figs. 2c and 2d; Table 1). The vertical reference planes in the 3D composition (Fig. 9) show associated columnar arrays, some extending over tens of microns or more. Other zones, such as the right-vertical panel in Fig. 9, show orthogonal interruptions of these columnar arrays as a consequence of beam scan anomalies. These microstructural/architectural features are shown in more detail in the transmission electron microscope (TEM) 3D image composition in Fig. 10 where the horizontal and vertical cellular and connected columnar arrays are observed to be composed of copper oxide (Cu_2O) cubic precipitates in an interconnected dislocation microstructure. The Cu_2O precipitates range in size from roughly 25 nm to 100 nm. These microstructural features are more clearly delineated in the magnified TEM vertical plane image shown in Fig. 11. The white zones shown by arrows represent Cu_2O precipitates which have been selectively dissolved by the acid-based electrolyte used to prepare the electron-transparent thin films for TEM observation (Fig. 11)^[7]. Fig. 10 appears to be represented by the columnar growth schematic shown in Fig. 2d. The Cu_2O precipitates occur initially in the atomized Cu precursor powder (Fig. 4b), and are also formed in the EBM fabrication process by incorporating the trace amounts of oxygen in the EBM vacuum environment.

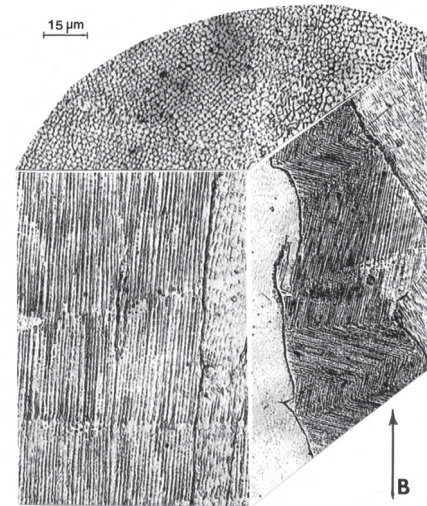


Fig. 9 3D LOM image composition for EBM fabricated Cu cylindrical monolith showing regular and irregular columnar arrays. The build direction is noted by B (arrow). Adapted from Martinez *et al.*^[14]

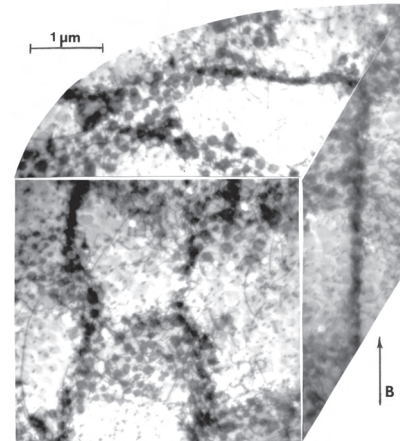


Fig. 10 Magnified 3D TEM image composition for EBM fabricated Cu cylindrical monolith shown in Fig. 9. The build direction is noted by B (arrow). Adapted from Martinez *et al.*^[14]

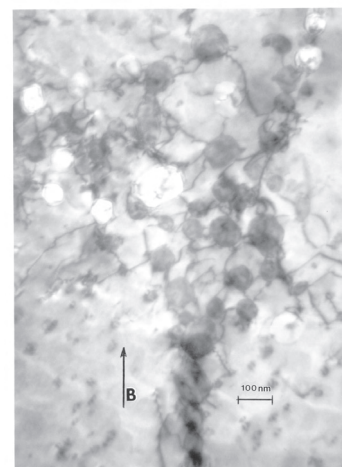


Fig. 11 Magnified TEM vertical build plane image showing Cu_2O precipitate-dislocation arrays. The build direction is shown by arrow at B

4.2 SLM Fabricated 17-4 PH Stainless Steel

In contrast to the copper monoliths as illustrated in Figs. 9 to 11, Fig. 12 shows a significantly different directional microstructure for SLM (Ar atmosphere) fabricated 17-4 PH (precipitation-hardened) stainless steel cylindrical monoliths (having a pre-alloyed powder composition of 16 Cr, 4 Ni, 4 Cu, <1% Mn, Si, Nb; balance Fe in weight percent; atomized in Ar). This microstructure is characterized by oriented (textured) α -Fe columnar grains as illustrated schematically in Fig. 2c. These grains are heavily dislocated as shown in the magnified 3D-TEM image composition in Fig. 13, while the XRD spectra shown in Fig. 14 illustrate the very strong $[200]_{\alpha}$ orientation in the horizontal reference plane in Figs. 12 and 13, and a corresponding $[110]_{\alpha}$ texture orientation in the vertical reference plane. Because the SLM fabricated component section represented in Fig. 12 is primarily the α -Fe phase (bcc ferrite, $a = 2.86 \text{ \AA}$), as shown in Fig. 14, the fabricated monoliths are highly magnetic, and correspond to traditional 17-4 PH stainless steel fabrication where the hardness is around Rockwell C-scale (HRC) 30^[13,23]. However, upon temper treatment at 482°C (900°F; referred to as H900 temper) for 1 hour and air cooled, copper precipitation elevates the hardness to slightly more than HRC 40^[13], which also coincides with contemporary 17-4 PH stainless steel temper treatment^[23-25].

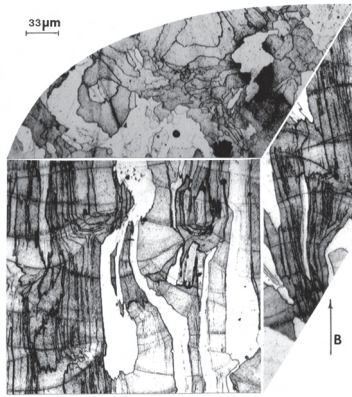


Fig. 12 3D LOM image composition for SLM (Ar atmosphere) fabricated 17-4 PH stainless steel component showing columnar, strongly textured α -Fe (martensite) grains. Build direction is shown by B. Adapted from Martinez *et al.*^[14]

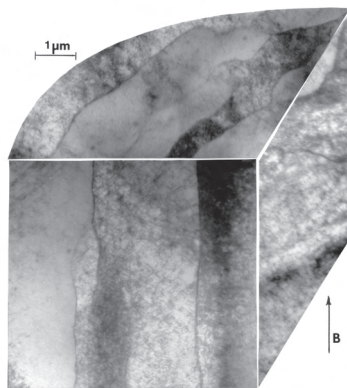


Fig. 13 Magnified 3D TEM image composition for SLM fabricated 17-4 PH stainless steel shown in Fig. 12. Build direction is shown by B. Adapted from Martinez *et al.*^[14]

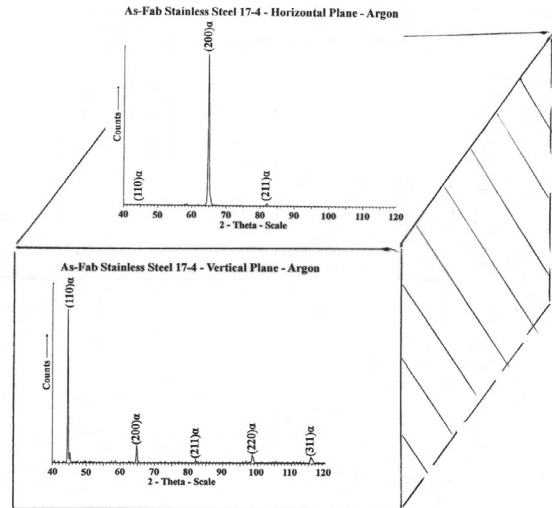


Fig. 14 XRD spectra illustrating strong (200) horizontal plane texture and (110) vertical plane texture for SLM (argon) fabricated 17-4 PH stainless steel in Figs. 12 and 13

4.3 EBM Fabricated Co-Base Superalloy

Fig. 15 shows, for comparison with Fig. 9, a 3D LOM image composition for a Co-26Cr-6Mo-0.2C superalloy monolith fabricated by EBM^[6]. While Fig. 9 shows columns of Cu_2O cubic precipitates, Fig. 15 shows columns of Cr_{23}C_6 cubic (fcc: $a = 10.66 \text{ \AA}$) precipitates. These precipitates are shown magnified in the 3D TEM image composition in Fig. 16 and the TEM vertical plane column view shown in Fig. 17. Stacking faults in the Co-Cr fcc ($a = 3.56 \text{ \AA}$) matrix are indicated by open arrows in both Figs. 16 and 17. The Cr_{23}C_6 precipitate columns appear to form primarily in the melt pool center as shown schematically in Fig. 2c. Irregularities in the scanning beam create irregularities in the directional, columnar precipitate arrays in Fig. 15 as in Fig. 9 for Cu prototypes. As noted in Fig. 9 for Cu, the EBM fabrication of Co-26Cr-6Mo-0.2C alloy is characterized by regular cell-like arrays corresponding to the melt pool dimensions in the horizontal reference plane, perpendicular to the build direction as shown in Fig. 15.

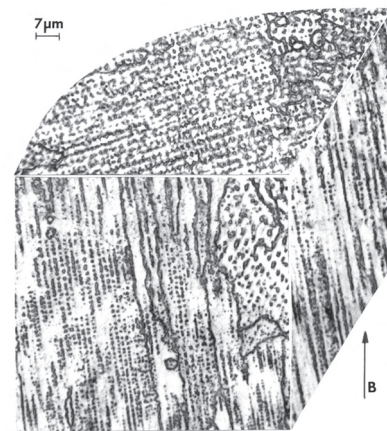


Fig. 15 3D LOM image composition for Co-base superalloy fabricated by EBM showing columnar Cr_{23}C_6 precipitate arrays. Arrow at B shows build direction

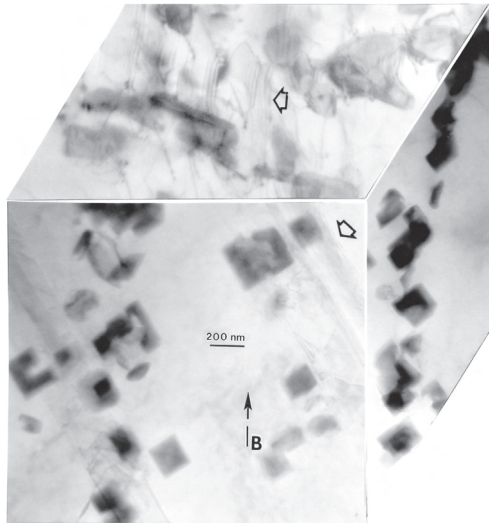


Fig. 16 3D TEM image composition for Co-base superalloy shown in Fig. 15. Open arrows show stacking faults on $\{111\}$ in the Co-Cr fcc matrix. Cubic Cr_{23}C_6 precipitate morphologies are apparent. The build direction is noted by arrow at B

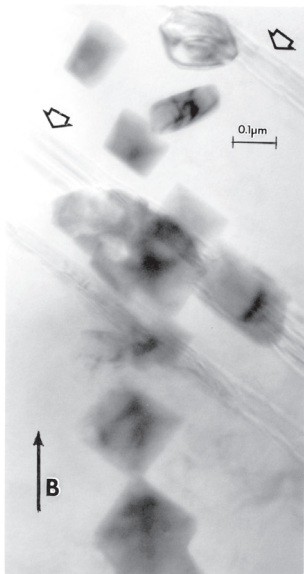


Fig. 17 Magnified TEM vertical section view showing Cr_{23}C_6 cubic precipitate column. Open arrows show $\{111\}$ stacking faults in the Co-Cr fcc matrix. The average precipitate dimension is ~ 100 nm. Arrow at B shows build direction which is essentially parallel to the columnar precipitate arrays

4.4 SLM Fabricated Inconel 718 (Ni-Base Superalloy)

Fig. 18 shows, for comparison with Figs. 9 and 15, columnar precipitate arrays resulting from SLM fabrication in contrast to EBM fabrication. The SLM process for Fig. 18 utilized a nitrogen atmosphere (Fig. 2b). The pre-alloyed, Inconel 718 precursor powder had a nominal composition consisting of 53.5% Ni, 19% Cr, 18.3% Fe, 5% Nb, 3% Mo, 1% Ti, and 0.43% Al (in weight percent). XRD spectra for the powder revealed it to be γ -fcc NiCr ($a = 3.59$ Å; Space Group: Fmm). This crystal structure also characterized the matrix for the fabricated components shown typically by the 3D LOM image composition in Fig. 18.

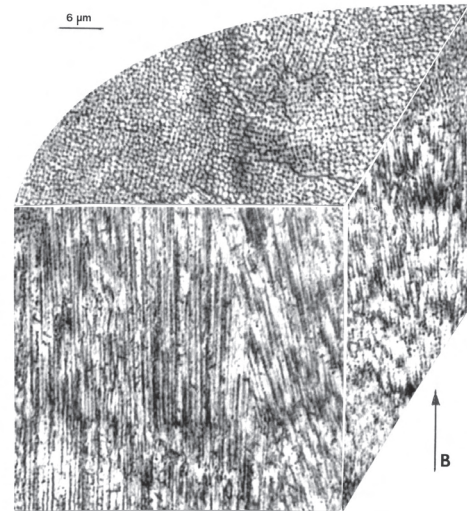


Fig. 18 3D LOM image composition for Inconel 718 cylindrical (Z-axis) component fabricated by SLM in nitrogen atmosphere

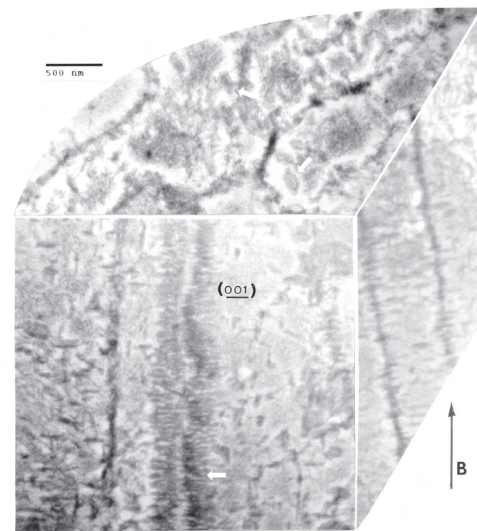


Fig. 19 3D TEM image composition showing coincident γ'' (Ni_3Nb) oblate spheroid precipitates in a representative volume segment from Fig. 18. B denotes the build direction. White arrows show precipitate morphologies

Fig. 19 shows a magnified, 3D TEM image composition corresponding to a section of Fig. 18 illustrating the γ'' - Ni_3Nb (bct: $a = 3.62$ Å, $c = 7.41$ Å) DO_{22} oblate spheroid precipitates coincident with the γ -fcc matrix $\{001\}$ planes: $(001) \gamma'' \parallel \{001\} \gamma^{[9,26,27]}$. These features are more readily observed on comparing the horizontal plane section views of the precipitates at white arrows in Fig. 19, along with the vertical section view of columnar precipitates shown by the white arrow in the vertical front face of Fig. 19. A higher magnification view of the oblate spheroid-shaped γ'' precipitates is provided in Fig. 20 which shows a lower magnification insert slightly rotated for different contrast. The coincidence with the (100) planes is noted while the surface orientation in the vertical plane in Figs. 19 and 20 is (200) , while the coincident plane for the precipitates is (001) . The (200) orientations in the horizontal and vertical plane sections are illustrated in the XRD spectra of Fig. 21.

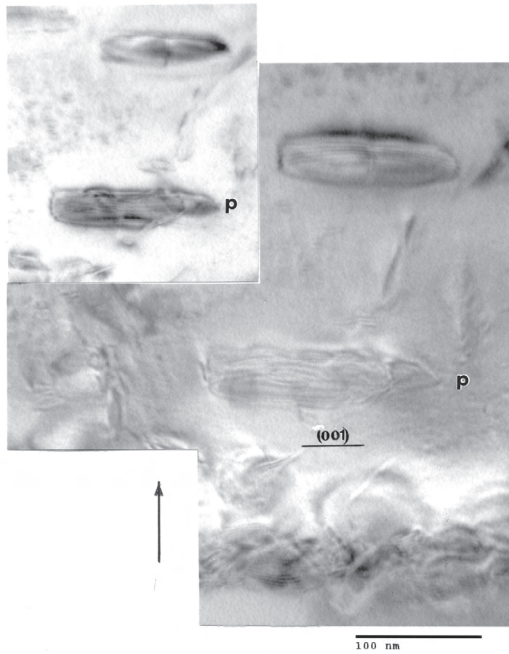


Fig. 20 Magnified TEM image views of γ'' oblate spheroid precipitates in Fig. 19 in the vertical reference plane parallel to the build direction (arrow). The γ -fcc matrix (001) plane is shown. The insert shows a tilted, lower magnification view of precipitates designated p

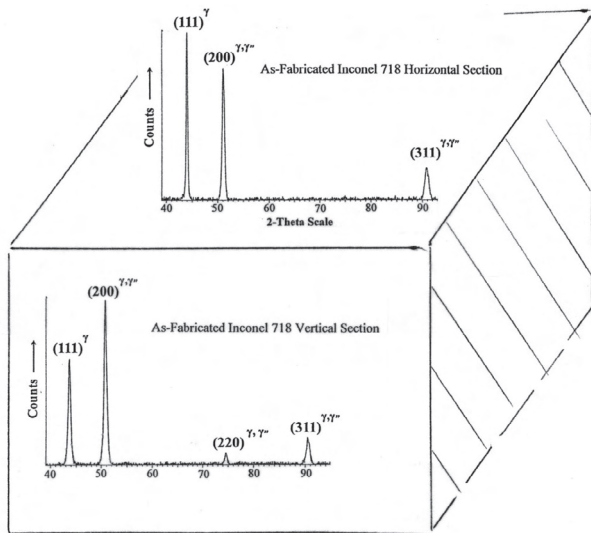


Fig. 21 XRD spectra corresponding to the horizontal and vertical (3D) reference frames in Figs. 19 and 20. The γ'' and γ peaks coincide as noted

It can be noted in Fig. 19 that the melt pool array features correspond to cell-like arrangements of the γ'' precipitates having an average dimension of $\sim 1 \mu\text{m}$. However, precipitates, as shown by the white arrows, also occur within these cell-like centers, which appear to contain very tiny precipitate clusters in addition to the oblate spheroid precipitate discs having a long dimension of 100 nm to 200 nm a minor (shorter) dimension of 75 nm to 125 nm, and a thickness of ~ 30 nm. Similar γ'' precipitate column architecture was also observed by Strondl *et al.* [28] for EBM-fabricated Inconel 718, but their study did not include detailed TEM analysis as illustrated in Figs. 19 and 20.

4.5 EBM and SLM Fabricated Inconel 625 (Ni-Base Superalloy)

Figs. 22 and 23 show 3D LOM and TEM image compositions, respectively for cylindrical prototypes fabricated by EBM in the Z-axis (cylinder axis) direction (the build direction B parallel to the cylinder axis) from pre-alloyed Inconel 625 precursor powder (66% Ni, 21% Cr, 9% Mo, 4% Nb, 0.4% Fe, traces of C and Ti; in weight percent). The average powder diameter was $\sim 22 \mu\text{m}$. It can be noted in both Figs. 22 and 23 that γ'' precipitate discs, similar to the oblate spheroids in the SLM fabrication of alloy 718 in Figs. 19 and 20, are coincident with the γ -fcc NiCr matrix, however the coincidence is $(001)\gamma'' \parallel \{111\}\gamma$, rather than $\{100\}$ [8]. These columnar γ'' Ni₃Nb (bct) precipitate arrays are associated with columnar grain boundaries (Fig. 23) as well as columns originating within the melt zone. The γ'' precipitates shown in Figs. 22 and 23 are more plate-like with dimensions of ~ 0.5 - $2 \mu\text{m}$, and thicknesses ranging from 15 nm-25 nm.



Fig. 22 3D LOM image composition for EBM fabricated Z-axis oriented Inconel 625 cylinder. Build direction is denoted B

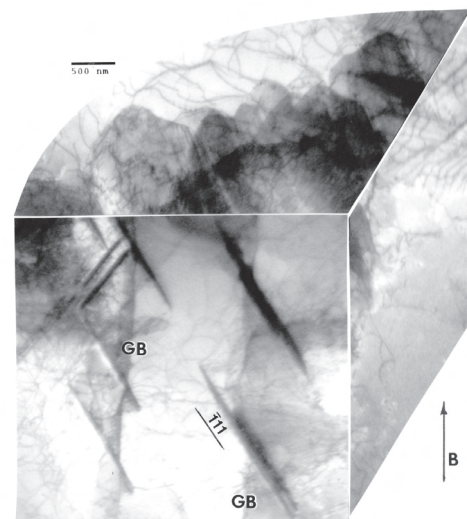


Fig. 23 3D TEM image composition showing $\{111\}\gamma$ coincident γ'' Ni₃Nb precipitate platelets corresponding to Fig. 22. Note dislocations associated with the precipitates. The precipitate columns in the front vertical reference plane coincide with low angle, columnar grain boundaries (GB). Build direction is denoted B

The XRD spectra in Fig. 24 show strong texturing of (200) in the horizontal reference plane and (220) in the vertical reference plane. When the EBM-fabricated components illustrated in the 3D microstructural architecture views of Figs. 22 and 23 are subjected to HIP treatment at 1,120°C for 4 hours in 0.1 GPa pressure Ar, the γ'' Ni₃Nb precipitates dissolve and the microstructure reverts to an equiaxed, Ni-Cr fcc grain structure with a high fraction of annealing twins and globular precipitates of primarily NbCr₂ (laves) precipitates (hexagonal: $a = 4.95 \text{ \AA}$, $c = 8.06 \text{ \AA}$), and some Cr precipitates^[8]. These features are illustrated in the corresponding 3D image composition shown in Fig. 25. Similar recrystallization and fcc equiaxed grain formation also occur for the EBM fabrication and HIP of the Co-base superalloy shown in Fig. 15 where the Cr₂₃C₆ carbide precipitate columns dissolve and are re-precipitated in the resulting equiaxed Co-Cr fcc grain boundaries^[6].

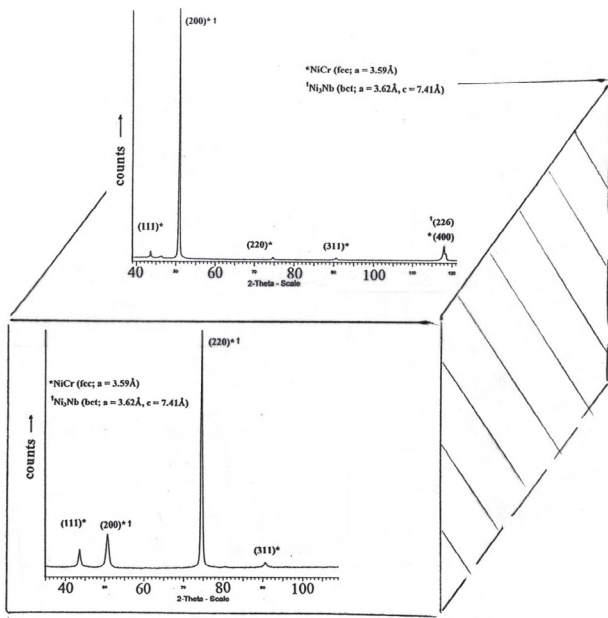


Fig. 24 XRD spectra corresponding to the horizontal and vertical (3D) reference frames in Figs. 22 and 23. The γ'' and γ peaks coincide as noted

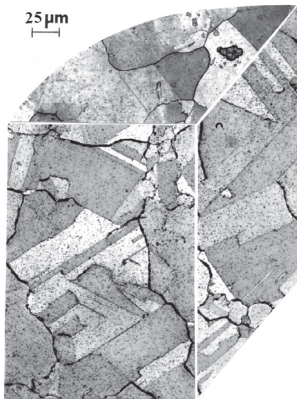


Fig. 25 3D LOM image composition for EBM-fabricated and HIPed Inconel 625 cylindrical (Z-axis) component showing equiaxed fcc grains with numerous coherent annealing twins containing numerous, homogenous distribution of precipitates

In contrast to Fig. 22 for EBM fabrication of Inconel 625 superalloy, Fig. 26 shows a corresponding 3D image composition for SLM fabrication of Inconel 625 in a nitrogen atmosphere (Fig. 2b). In contrast to Fig. 22, the cylindrical component represented in Fig. 26 was oriented in the powder bed plane (x - y plane), and the build direction shown in Fig. 26 (arrow at B) was perpendicular to the cylinder axis. This produced a somewhat more rapid cooling which contributed to the SLM process cooling as a consequence of the more rapid beam scan rate. In contrast to Fig. 22 for EBM processing, the SLM processed component represented by Fig. 26 is considerably different, although columnar precipitation corresponding to the same spatial dimensions are apparent. Also apparent is the prominent melt scan bonding which appears in Fig. 26 just below V. This bending is shown in more detail in the lower magnification vertical reference plane view shown in Fig. 27, and represents the apparent layering. Fig. 27 also demonstrates the irregularity in the columnar microstructures which are also somewhat apparent in the higher magnification view in Fig. 26. The contrast provided to illustrate the melt bonds in Figs. 26 and 27 arises from γ'' precipitates concentrating in these regions. The 3D TEM image composition in Fig. 28 shows, in contrast to Fig. 23, that the γ'' precipitates for SLM fabrication of alloy 625 occur as globular, nano particles in dense directional dislocation arrays. These γ'' nano particles range in size from ~30 nm-70 nm.

Fig. 29 shows, in comparison with Fig. 25, that HIPing of the SLM-fabricated component represented by Figs. 26 to 28 dissolves the γ'' (Ni₃Nb) nano particle precipitates (Fig. 28), and produces an equiaxed, Ni-Cr fcc grain structure containing a high fraction of annealing twins and globular precipitates in both the grain interiors and the grain boundaries. In contrast to the NbCr₂ (laves) and some Cr precipitates which form in the HIPed, EBM-fabricated alloy 625 shown in Fig. 25, the precipitates in Fig. 29 are dominated by MoNb (bcc, $a = 3.20 \text{ \AA}$) and some Nb₃Ni precipitates, along with a small fraction of NbCr₂ precipitates^[29]. Consequently, the microstructures or especially the nature of the columnar γ'' (Ni₃Nb) precipitates differ morphologically for

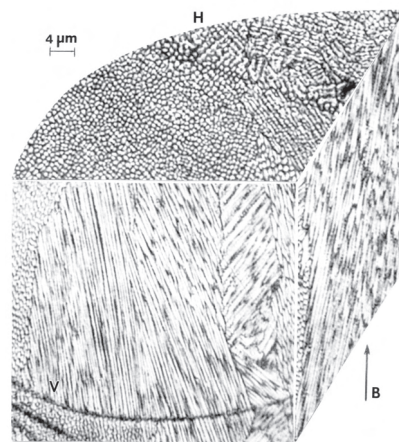


Fig. 26 3D LOM image composition for SLM fabricated x , y axis oriented Inconel 625 cylinder. Build direction is shown at B. H and V indicate horizontal and vertical reference planes, respectively which are correspondingly perpendicular to and parallel to the build direction, respectively. Adapted from Amato *et al.*^[29]



Fig. 27 3LOM low-magnification vertical reference plane view for SLM-fabricated Alloy 625 (Fig. 26) showing melt bands and irregular columnar arrays. Build direction is shown by white arrow at B

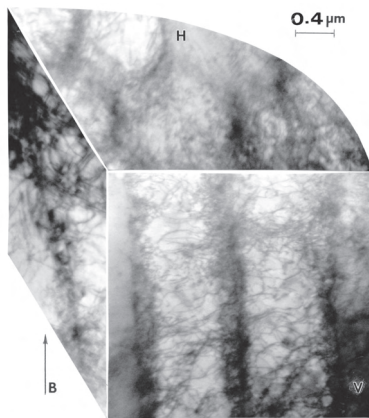


Fig. 28 3D TEM image composition corresponding to Fig. 26 showing columnar dislocation structures and γ'' nano particle precipitates. H and V denote horizontal and vertical reference planes. B denotes the build direction. The vertical plane orientation was (110); consistent with Fig. 23

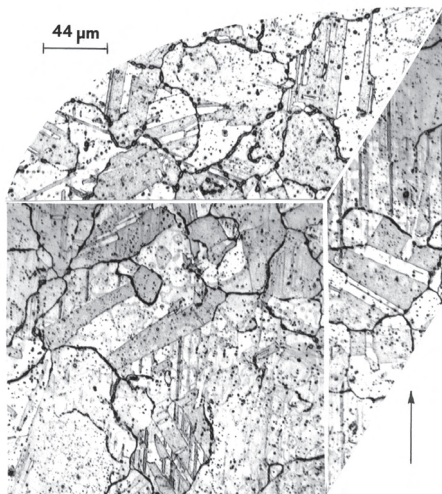


Fig. 29 3D LOM image composition for SLM-fabricated and hiped Inconel 625 cylindrical (x, y axis) component showing equiaxed fcc grains with numerous annealing twins containing numerous, homogeneous distribution of precipitates. The original build reference is shown by the arrow

EBM fabrication of alloy 625 (Figs. 22 and 23) in contrast to SLM fabrication (Figs. 26 and 28). Correspondingly, the re-precipitation after HIP treatment of the as-fabricated alloy 625 also changes: dominated by NbCr_2 (laves) precipitates in the case of the EBM fabrication plus HIP (Fig. 25) in contrast to MoNb precipitates in the case of the SLM fabrication plus HIP (Fig. 29).

4.6 Comments on Mechanical Properties for EBM and SLM Fabricated Products: Hardness

On examining the EBM and SLM-fabricated components reviewed herein, it might appear that those exhibiting obvious, directional microstructures and microstructural architectures may exhibit directional or asymmetric mechanical responses. It can be observed in Figs. 6 and 7 that the horizontal and vertical reference plane hardnesses differ by roughly 15% while there is no obvious texture or directional microstructure. However, in the case of apparent directional microstructures in Cu as shown in Fig. 9, the horizontal plane hardness is roughly 7% softer than the corresponding vertical plane hardness as shown in Table 2, and consistent with Figs. 6 and 7. Similarly, many of the other EBM and SLM-fabricated components exhibit in directional microstructures (Figs. 12, 15, and 18, for example) do not show similar variances between the horizontal plane (H) and vertical plane (V) hardnesses, attesting to the fact that there are no prominent directional hardness responses for either EBM or SLM-fabricated products considering a range of metals and alloys (Table 2). It must be noted that the horizontal and vertical microstructure length scales are essentially the same, as determined by the beam scan parameters, and this dimensional feature, which often controls more conventional microstructures, may dominate. This feature is apparent on comparing Figs. 6, 7, and 8 where phase dimensions govern the hardness. Nonetheless, the EBM and SLM fabricated components emulate the hardness response for representative wrought and cast products (Table 2).

Since EBM and SLM fabrication of metal and alloy products is in its infancy, the systematic study of microstructures and microstructural architectures produced by varying build parameters as well as specific alloy component compositions may exhibit novel and controllable mechanical properties just as more conventional processing has allowed for structure-property manipulations.

5. Discussion and Closure

This review has attempted to provide a brief but comparative overview of electron and laser beam melting technologies applied to a range of metal and alloy fabrication. In addition, we have drawn upon our own recent research work in providing a number of comparative 3D LOM and TEM (isometric) image compositions which allow microstructural and microstructural architecture (especially columnar and related directional arrays) to be visualized in the context of the 3D additive EBM and SLM processes which are central to this presentation. Although we have not specifically emphasized the characterization of resulting directional microstructures in the context of more conventional processing of the metals and alloys discussed (such as

Table 2 Hardness Comparisons for EBM and SLM Fabricated Metals and Alloys

System Fabricated	Z-axis orientation		X-Y orientation		Commercial wrought	Commercial cast
	Horizontal (H)*	Vertical (V)*	Horizontal (H)*	Vertical (V)*		
aTi-6Al-4V: EBM	HV: 4.2 GPa HRC: 45	HV: 3.5 GPa HRC: 42	—	—	HV: 4.1 GPa HRC: 50	HV: 3.5 GPa
Ti-6Al-4V: SLM	HV: 4.3 GPa HRC: 46	HV: 4.0 GPa HRC: 44	—	—	—	—
Cu: EBM	HV: 0.81 GPa	HV: 0.87 GPa	—	—	Anneal HV: 0.57 GPa	—
Co-base alloy: EBM (Co-Cr alloy)	HV: 4.5 GPa HRC: 47	HV: 4.6 GPa HRC: 48	—	—	—	ASTM F-75 Annealed HRC: 25-35**
Inconel 625: EBM	HV: 2.8 GPa HRC: 14	HV: 2.5 GPa HRC: 13	—	—	HRC: 40 Anneal HRC: 20	—
Inconel 625: SLM	HV: 3.9 GPa HRC: 40	HV: 4.1 GPa HRC: 45	HV: 4.0 GPa HRC: 40	HV: 4.4 GPa HRC: 45	—	—
17-4 PH Stainless: SLM	HV: 3.8 GPa H900 HV: 6.1 GPa [†] HRC: 29 H900 HRC: 43 [†]	HV: 3.8 GPa H900 HV: 6.1 GPa [†] HRC: 29 H900 HRC: 43 [†]	—	—	HRC: 35 H900 HRC: 45 [†]	—
Inconel 718: SLM	HV: 5.6 GPa HRC: 38	HV: 5.8 GPa HRC: 39	HV: 5.4 GPa HRC: 38	HV: 5.6 GPa HRC: 35	Annealed HRC: 24 Aged HRC: 40	—

*Note that the horizontal reference plane is perpendicular to the build direction while the vertical reference plane is parallel to the build direction. Samples built in the Z-axis orientation are parallel to the build direction while those in the x-y orientation are normal or perpendicular to the build direction.

**The annealed, EBM-fabricated products produce similar hardness values^[6].

[†]H900 anneal: Anneal at 900°F for 1h.^[13,23,24] Note that hardnesses are given as HV (Vickers) microindentation measurements and HRC (Rockwell C-scale macro-hardness measurements).

casting and forging), it should be apparent that both EBM and SLM provide a new directional solidification paradigm. The significance of this new paradigm is certainly apparent on comparing, in retrospect, the 3D LOM and TEM image compositions for Ti-6Al-4V (Figs. 6 and 7), Cu (Figs. 9 and 10), 17-4 PH stainless (Figs. 12 and 13), Co-base superalloy (Figs. 15 and 16), Inconel 718 (Figs. 18 and 19), and Inconel 625 (Figs. 22 and 23; 26 and 28). Taken together, these 3D image compositions and selected XRD components (Figs. 14, 21 and 24) provide contemporary examples of what is referred to as 3D materials science; as it applies to advanced manufacturing technology in the context of 3D-additive processing. This allows for effective visualization of 3D microstructures and microstructural architectures arising for directional solidification phenomena, and permits the conclusions noted in Section 4.6 above regarding hardness diagnostics.

Acknowledgements

This research was supported in part by Mr. and Mrs. MacIntosh Murchison Chair Endowments at the University of Texas at El Paso. Portions of this work were also supported by Lockheed-Martin Aeronautics, Marietta, GA. We are grateful to Shane Collins of Directed Manufacturing, Austin, Texas for providing several SLM specimens for study and analysis.

REFERENCES

- Hunt DV. Dictionary of advanced manufacturing technology. New York: Elsevier, 1987.
- Chuna CK, Leong KF, Lin CS. Rapid prototyping: Principles and applications. 2.ed. Singapore: World Scientific, 2003.
- Gibson I, Rosen DW, Stucker B. Additive manufacturing technologies: Rapid prototyping to direct digital manufacturing. New York: Springer, 2010.
- Grenda E. Printing the future: The 3D printing and rapid prototyping source book. 3.ed. Arlington, MA: Castle Island Co., 2010.
- Murr LE, Quinones SA, Gaytan SM, Lopez MI, Rodela A, Martinez EY *et al.* Microstructure and mechanical behavior of Ti-6Al-4V for biomedical applications produced by rapid-layer manufacturing. *J Mech Behav Biomed Mater* 2009; 2(1): 20-32.
- Gaytan SM, Murr LE, Martinez E, Martinez JL, Machado BI, Ramirez DA *et al.* Comparison of microstructures and mechanical properties for solid and mesh cobalt base alloy prototypes fabricated by electron beam melting. *Metall Trans A* 2010; 41A:3216-27.
- Ramirez DA, Murr LE, Li SJ, Tian E, Martinez E, Machado BI *et al.* Open-cellular copper structures fabricated by additive manufacturing using electron beam melting. *Mater Sci Engin A* 2011; 528A:5379-86.
- Murr LE, Martinez E, Gaytan SM, Ramirez DA, Machado BI, Shindo PW *et al.* Microstructural architecture, microstructures, and mechanical properties for a nickel base superalloy

- fabricated by electron beam melting. *Metall Trans A* 2011; 42A: 3491-508.
9. Amato KN, Gaytan SM, Murr LE, Martinez E, Shindo PW, Hernandez J *et al.* Microstructures and mechanical behavior for Inconel 718 fabricated by selective laser melting. *Acta Materialia* 2012. [In Press]
 10. Murr LE, Martinez E, Gaytan SM, Ramirez DA. Contributions of light microscopy to contemporary materials characterization: The new directional solidification. *Metallography, Microstructure and Analysis*. 2012. [In Press]
 11. Hernandez J, Murr LE, Gaytan SM, Martinez E, Medina F, Wicker RB. Microstructures for two-phase gamma titanium aluminum fabricated by electron beam melting. *Metallography, Microstructure and Analysis* 2012. [In Press]
 12. Murr LE, Gaytan SM, Ramirez DA, Martinez E, Hernandez J, Amato KN *et al.* Metal fabrication by additive manufacturing using laser and electron beam melting technologies. *JMST* 2012; 28(1):1-14.
 13. Murr LE, Martinez E, Hernandez J, Collins S, Amato KN, Gaytan SM *et al.* Microstructures and Properties of 17-4 PH stainless steel fabricated by selective laser melting. [To be published] 2012.
 14. Martinez E, Murr LE, Amato KN, Hernandez J, Shindo PW, Gaytan SM *et al.* 3D microstructural architectures for metal and alloy components fabricated by 3D printing/additive manufacturing technologies. *Proceedings of the 1st International Conference on 3D Materials Science*. Warrendale, PA, TMS. 2012 (CD format).
 15. Faubert FM, Springer GS. Measurement of the thermal conductivity of argon, krypton and nitrogen in the range 800-2000K. *Journal of Chemical Physics* 1972; 57:2333-40.
 16. Thijs L, Verhaeghe F, Craeghs T, Van Humbeeck J, Kruth J-P. A study of the microstructural evolution during selective laser melting of Ti-6Al-9V. *Acta Materialia* 2010; 58:3303-12.
 17. Carson JW, Pittenger BH. Bulk properties of Powders in *ASM Handbook Vol. 7 - Powder Metal Technologies and Applications*, W.B. Eisen *et al.* (eds.). Materials Park, OH, ASM International 1998; pp. 287-301.
 18. Rumpf H, Herrmann W. Properties, bonding mechanisms and strength of agglomerates. *Processing Preparation* 1970; 11(3):117-27.
 19. Prescott JK, Barnum RA. On powder flowability. *Pharmaceutical Technology*. 2000; (October):60-85.
 20. Boulos MI. The inductively coupled R. F. plasma. *Journal of Pure and Applied Chemistry* 1985; 57:1321-52.
 21. Boulos MI. The inductively coupled radio frequency plasma. *Journal of High Temperature Materials Processes* 1997; 1:17-39.
 22. Boulos MI. Induction plasma processing of materials for powders, coatings, and near-net-shape parts. *Advanced Materials & Processes* 2011; (August):52-3.
 23. Roberts DA, Roach DB, Hall AM. *Physical and Mechanical Properties of Precipitation Hardenable Stainless Steels*. Washington, D.C.: Office of Technical Services, U.S. Department of Defense (Code PB15 1068); 1959.
 24. Rock HJ, Kalish D. The strength, fracture toughness, and low cycle fatigue behavior of 17-4 PH stainless steel. *Metallurgical Transactions* 1974; 5:1595-605.
 25. Murayama M, Katayama Y, Hono K. Microstructural evolution in a 17-4 PH stainless steel after aging at 400°C. *Metall Trans A* 1999; 30A:345-53.
 26. Cozar R, Pineau A. Morphology of γ' and γ'' precipitates and thermal stability of Inconel 718 type alloys. *Metall Trans A* 1973; 4(1):47-59.
 27. Sundararaman M, Mukhopadhyay P, Banerjee S. Some aspects of the precipitation of metastable intermetallic phases in Inconel 718. *Metall Trans A* 1992; 23A:2015-28.
 28. Strondl A, Fischer R, Frommeyer G, Schneider A. Investigations of MX and γ' and γ'' precipitates in the nickel-based superalloy 718 produced by electron beam melting. *Materials Science and Engineering A* 2008; 480A:138-47.
 29. Amato KN, Hernandez J, Murr LE, Martinez E, Gaytan SM, Shindo PW *et al.* Comparison of microstructures and properties for a Ni-base superalloy (Alloy 625) fabricated by electron and laser beam melting. *Journal of Materials Science Research* 2012; 1(2):3-41.